

Full Length Article

A computational map of the probe CO molecule adsorption and dissociation on transition metal low Miller indices surfaces

David Vázquez-Parga^a, Anabel Jurado^a, Alberto Roldan^{b,*}, Francesc Viñes^{a,*}^a Departament de Ciència de Materials i Química Física & Institut de Química Teòrica i Computacional (IQTCUB), Universitat de Barcelona, c/Martí i Franquès 1, 08028 Barcelona, Spain^b Cardiff Catalysis Institute, School of Chemistry, Cardiff University, Park Place, Cardiff CF10 3AT, Wales, UK

ARTICLE INFO

Keywords:

DFT
Transition metal surfaces
CO
Adsorption
Dissociation
Descriptors

ABSTRACT

The adsorption and dissociation of carbon monoxide (CO) have been studied on 81 Transition Metal (TM) surfaces, with TMs having body centred cubic (*bcc*), face centred cubic (*fcc*), or hexagonal close-packed (*hcp*) crystalline structures. For each surface, CO, C, and O adsorptions, and C+O co-adsorptions were studied by density functional theory calculations on suited slab models, using the Perdew-Burke-Ernzerhof functional with Grimme's D3 correction for dispersive forces. CO dissociation activation and reaction energies, ΔE , were determined. The values, including zero point energy, were used to capture chemical trends along groups, *d*-series, and crystallographic phases concerning CO adsorption and dissociation, while simulated infrared (IR) spectroscopies and thermodynamic phase diagrams are provided. Late *fcc* TMs are found to adsorb CO weakly, perpendicularly, and are IR-visible, opposite to early *bcc* TMs, while *hcp* cases are distributed along these two extremes. The *d*-band centre, ϵ_d , is found to be the best descriptor for CO adsorptions and C + O co-adsorptions, ΔE , and activation energies. The implications of the found trends and descriptors are discussed on processes requiring CO dissociation, such as the Fischer-Tropsch.

1. Introduction

Transition Metals (TMs) are ubiquitous materials employed in a myriad of industrially and technologically relevant fields. These range from energy storage devices [1], through drug release nanotechnologies [2], to heterogeneous catalysis [3], to name a few. The interaction of carbon monoxide (CO) with catalytic TM surfaces has been extensively studied in the past due to its importance to chemical industries [4–6]. The CO properties paved the way to its use as a probe molecule to obtain atomistic information on the studied surfaces upon CO adsorption [7–9]. Besides its use as a probe molecule in the field of Surface Science, it is also used as a reactant, e.g., in the Fischer-Tropsch (FT) process, generating hydrocarbons from CO:H₂ mixtures [10], a key ingredient for the carbon circular economy when CO is generated from previously captured and dissociated carbon dioxide (CO₂). Aside, CO is a sought product, for instance, through the reverse water gas shift reaction, where CO₂ can be revalued by reacting with H₂ to yield CO and H₂O (CO₂ + H₂ → CO + H₂O, $\Delta H_r^\circ = 41 \text{ kJ}\cdot\text{mol}^{-1}$) [11], with the concomitant environmental implications in the fight against global warming and climate change. Apart from these, the CO molecule can be a key intermediate, e.

g. as in the course of CO₂ hydrogenation towards methanol fuel, again key in making carbon economy circular [12]. Thus, the interaction of CO with TM-based catalysts has gained importance as a way, not only to gain atomistic insights of the latter using CO as a probe molecule, but also as a crucial species in diverse processes of industrial and environmental relevance.

Thus, a systematic investigation of the CO interaction with TMs and its possible dissociation would not only allow the discovery of the key, acting descriptors unfolding the physicochemical properties of TM surfaces and set a predicting basis for complex systems, e.g. TM nanoparticles [13] and bimetallic structures [14], but could also drive the description of single-atom alloys, which have become a hub of research in the recent years [15,16]. Such an understanding could be gained by means of Surface Science techniques [17], yet experimental methods suffer from limitations and inaccuracies, e.g. having the need of using well-characterized single-crystal metal surfaces, a ultra-high vacuum chamber while controlling the dose of CO, and the unavoidable acquirement of mean, average information of all the molecules and active sites present on the sample. A suitable alternative to gain molecular and site-specific atomistic information is the use of accurate

* Corresponding authors.

E-mail addresses: roldanmartineza@cardiff.ac.uk (A. Roldan), francesc.vines@ub.edu (F. Viñes).<https://doi.org/10.1016/j.apsusc.2023.156581>

Received 4 November 2022; Received in revised form 11 January 2023; Accepted 25 January 2023

Available online 3 February 2023

0169-4332/© 2023 The Author(s). Published by Elsevier B.V. This is an open access article under the CC BY license (<http://creativecommons.org/licenses/by/4.0/>).

atomistic simulations. Within this Computational Surface Science field, Density Functional Theory (DFT) applied to surface slab models has excelled over other approaches, being an excellent compromise in between computational cost and accuracy.

Herein we thoroughly investigate the CO molecule adsorption and breakage processes on TM surfaces to unfold the most prominent trends, driving forces, and chemical descriptors in a broad, general fashion. To this end, the CO adsorption is systematically studied by DFT means on all 3d, 4d, and 5d TMs displaying regular face-centred cubic (*fcc*), body-centred cubic (*bcc*), or hexagonal close-packed (*hcp*) crystallographic structures, accounting for 27 different TMs. The three lowest-index Miller surfaces from each TM are analyzed, accounting in all cases for the most stable regular surfaces [18], *i.e.* without featuring step edges. These are (001), (011), and (111) surfaces for both *fcc* and *bcc* TMs, and (0001), (10 $\bar{1}$ 0), and (11 $\bar{2}$ 0) surfaces for *hcp* TMs, see Fig. 1, making up 81 studied TM surfaces.

2. Computational details

The adsorption and dissociation of the CO molecule on the aforementioned 81 TM surfaces have been evaluated through periodic DFT calculations, as implemented in the Vienna *Ab-Initio* Simulation Package (VASP) code [19]. Projector Augmented Wave (PAW) pseudopotentials have been used to describe core electrons density and its interaction with the valence electron density [20]. For the DFT calculations, the Perdew-Burke-Ernzerhof (PBE) exchange–correlation functional was chosen [21], known to be among the most suited and accurate in the description of both bulk and surface TM properties [22]. For the better description of the long-range, dispersive forces interactions, Grimme’s D3 correction has been accounted in the calculations [23], previously proven to deliver results comparable to the more-grounded many-body dispersion [24]. DFT PBE-D3 calculations have shown accuracy in determining CO adsorption site preference and bond strength trends on TM surfaces [25], yet is still also known to fail in few particular yet

notable cases, like the ‘CO/Pt(111) puzzle’ [26], where CO should occupy a top position, while standard DFT favours occupancy of *fcc* hollows, due to an unduly placement of CO frontier orbitals with respect to the Pt band structure [27], a deficiency solvable when using hybrid functionals, and attenuated when adding dispersive forces [28].

The TM surfaces were represented by six-layered supercell slab models, previously optimized so as to deliver slab-width converged results [29]. During the DFT optimizations, the three bottommost layers were kept frozen to represent the materials bulk, while the topmost three layer were allowed to fully relax, along with the adsorbed CO molecule, or the adsorbed C or O adatom moieties, *i.e.* 3+3 approach. The slab models had a vacuum of 10 Å perpendicular to the modelled surface to prevent any spurious interactions between the periodically repeated layers. The supercells size was adjusted to maintain similar CO coverage between different surfaces. Thus, (3×3) supercells were used for *fcc* (111) surfaces, *bcc* (001) and (111) surfaces, and *hcp* (10 $\bar{1}$ 0) surface, having nine atoms per layer, see Fig. 1. On the other hand, (2×2) supercells were employed for *fcc* (001) and (011) surfaces, *bcc* (011) surface, and *hcp* (0001) and (11 $\bar{2}$ 0) surfaces, see Fig. 1, having eight atoms per layer. Thus, the resulting coverage of all the surfaces resulted in similar $1/8$ or $1/9$ of a monolayer (ML), depending on the number of metallic atoms forming each layer. This allows focusing the study and analysis on the CO interaction with the TM surfaces only, safely neglecting the effect of lateral interactions by having a low surface coverage. However, one has to keep in mind that significant changes are to be expected in CO adsorption energies, site preference and conformation, CO stretching vibrational frequency, and CO dissociation energy change and energy barriers when having significantly larger coverages, as found *e.g.* on Pt (111) surface [30], or regular Fe (100), (110) and (111) surfaces [31].

The CO molecule was sampled and relaxed on each of the 81 TM surfaces, starting from a height of 2 Å for the CO atom closest to the TM surface, and with the CO molecule placed on highly symmetric positions, see Fig. 1 and Figs. S1-S3 of Section S1 of the Supplementary Material

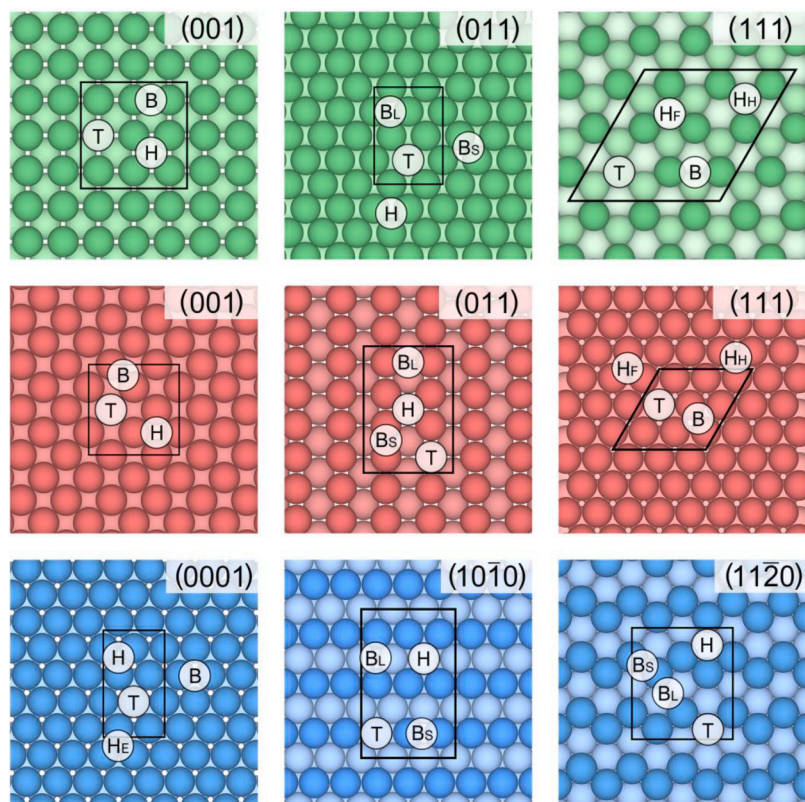


Fig. 1. Top view of the nine different studied TM surfaces according to their *fcc* (red spheres), *bcc* (green spheres), and *hcp* (blue spheres) crystallographic structures. Dark (light) coloured spheres denote surface (subsurface) metal atoms. For each surface, high-symmetry sites are pointed out, including standard top (T) and bridge (B) sites, but also short (B_s) and long (B_l) bridge sites, fourfold hollow sites (H) on *bcc* and *fcc* (001) surfaces, *fcc* (011) surfaces, and *hcp* (10 $\bar{1}$ 0), and (11 $\bar{2}$ 0) surfaces, and threefold hollow sites on the rest of the surfaces, including *fcc* (H_f) and *hcp* (H_h) hollow sites on *bcc* and *fcc* (111) surfaces, threefold hollows (H) on *bcc* (011) and *hcp* (0001), and hollow empty (H_e) in the *hcp* (0001) surfaces. Black lines denote the employed surface supercell.

(SM). This involved positions where the CO molecule laid perpendicular or parallel with respect to the surface plane. In the former, both orientations were examined, *i.e.*, connected through C or O atoms. Upon relaxation, the strength of the adsorption was quantified through the adsorption energy, E_{ads} , defined by the difference between the adsorbed system energy, E_{AS} , and those of the adsorbate in vacuum, E_A , and the clean surface, E_S ;

$$E_{ads} = E_{AS} - (E_A + E_S) \quad (1)$$

In all the employed slabs, the reciprocal space was sampled using optimized Monkhorst-Pack k -point meshes of $3 \times 3 \times 1$ dimensions. The geometric optimizations were carried out using a plane-wave basis set with a kinetic energy cutoff of 415 eV, enough to reach the chemical accuracy of ~ 0.04 eV as tested on adsorption energies, see below. The electron density optimization criterion was set to 10^{-6} eV, while atomic relaxation stopped when consecutive geometries yielded differences in energy below 10^{-5} eV. All calculations were considered closed shell, *i.e.* non-spin polarized, except for Co, Ni, and Fe magnetic surfaces [29]. The placed CO molecule was optimized likewise isolated in the centre of a $10 \times 10 \times 10 \text{ \AA}^3$ cubic unit cell and optimized at Γ -point. For evaluating the energy of isolated C and O atoms, the procedure was similar to the CO molecule but placed inside a $9 \times 10 \times 11 \text{ \AA}^3$ broken-symmetry unit cells, so as to force and gain their correct orbital occupancies.

For each of the most stable adsorption positions, vibrational frequency calculations were carried out by constructing and diagonalizing the Hessian matrix, built from finite displacements of atomic positions of 0.03 \AA in length. In these cases, only displacements of the CO molecular atoms were regarded, *i.e.* the CO molecule vibrations were treated decoupled from the TM surface phonons, since test calculations considering them yielded negligible changes in the gained vibrational frequencies at an exceedingly high computational cost. The obtained vibrational frequencies were used to characterize the situations as minima, *i.e.* without imaginary vibrational frequencies, and to correct adsorption energies by the Zero Point Energy (ZPE), gained as

$$ZPE = \frac{1}{2} \sum_i^{NMV} h\nu_i \quad (2)$$

where h is Planck's constant and ν_i is each computed vibrational frequency. Note that CO in vacuum has a single vibrational frequency, but when adsorbed, its free translational and rotational movements become frustrated, and effectively become vibrations. Thus, the adsorbed CO features six Normal Modes of Vibration (NMV). The changes in the dipole moment perpendicular to the surface associated with the estimated vibrations were used to simulate infrared (IR) spectra, accounting for the surface dipole selection rule, as extensively used in the past to correlate simulated and experimental IR spectra [32–34].

Since the presented equations would work for limit situations with zero temperature and CO pressure, thermodynamic phase diagrams were constructed to show the effect of temperature and CO pressure on its adsorption strength. To this end we employed the *Ab Initio* Thermodynamics (AIT) approach to calculate the free energy of adsorption, ΔG^{ad} [35], defined as:

$$\Delta G^{ad}(T, p_{CO}) \approx -\frac{1}{A} [E_{AS} + ZPE_{AS} - E_S - N_{CO}(E_{CO} + ZPE_{CO}) - N_{CO}\Delta\mu_{CO}(T, p_{CO})] \quad (3)$$

where A is the supercell surface area, E_{AS} the total energy of the metal surface with the adsorbed CO, E_S the energy of the pristine metal surface, ZPE_{AS} the ZPE energy of the adsorbed CO, N_{CO} the number of CO molecules adsorbed on the surface, E_{CO} the total energy of CO molecule in vacuum, and ZPE_{CO} the CO ZPE energy. The pressure, p , can be simplified as the pressure of the CO, p_{CO} . Finally, $\Delta\mu_{CO}$ is the variation of the CO chemical potential defined from statistic thermodynamics as a function of translational, rotational, vibrational, and electronic partition

functions, defined as

$$\Delta\mu_{CO}(T, p) = -k_B T \left\{ \ln \left[\left(\frac{2\pi m_{CO}}{h^2} \right)^{3/2} \frac{(k_B T)^{5/2}}{p_{CO}} \right] + \ln \left(\frac{k_B T}{\sigma_{CO}^{sym} B_{o,CO}} \right) - \sum_{i=1}^n \ln \left[1 - \exp \left(\frac{-h\nu_{i,CO}}{k_B T} \right) \right] + \ln(I_{CO}^{spin}) \right\} \quad (4)$$

where k_B is the Boltzmann's constant, m_{CO} is the mass of the CO molecule, σ_{CO}^{sym} is the classical symmetry number of the CO rigid molecule, B_o is the rotational constant, calculated as $\frac{h^2}{2I_{CO}}$, where h is the reduced Planck's constant, I_{CO} is the moment of inertia of the molecule, calculated as $\sum_i m_i r_i^2$ where m_i is the mass of each atom and r_i the distance of the atom to the centre of mass, and I_{CO}^{spin} is the electronic spin degeneracy of the ground state.

Furthermore, the CO dissociation energy was estimated by co-adsorbing a C adatom with an O adatom in its proximity. To this end, we profited from previous research on the stability of C atoms on the TM surfaces [35]. In addition, we explored the adsorption of O atoms likewise, sampling the same high symmetry sites as the perpendicular CO molecule, and using the O atom in vacuum as reference, modelled in the same box as the CO molecule, but spin-polarized to grant correct orbital occupancy, see Tables S1-S3 of Section S2 of the SM. Different combinations of C and O adatoms were optimized. Likewise, the lowest energy structures were characterized through vibrational frequency analysis, and the energies corrected with ZPE. Thus, the CO dissociation energy change, ΔE , is calculated as the difference between the energy with both C and O atoms adsorbed, E_{C+O} , with the energy of the CO molecule adsorbed, E_{CO} , both their respective ZPE;

$$\Delta E = (E_{C+O} + ZPE_{C+O}) - (E_{CO} + ZPE_{CO}) \quad (5)$$

Having characterized the initial and final states of the CO dissociation on the 81 TM surfaces, we extensively searched the CO dissociation reaction Transition States (TSs). To this end, the Improved Dimer (ID) [36] and Climbing-Image Nudged Elastic Band (CI-NEB) [37] methods were used. When necessary, *i.e.* when forces acting on the atoms in the TS were not sufficiently close to zero—implying that the found point is not a true stationary point of the potential energy surface—a Quasi-Newton optimization was carried out until forces were found to be below $0.03 \text{ eV} \cdot \text{\AA}^{-1}$. All the TSs were characterized as saddle points by vibrational frequency analysis, this is, with a single imaginary frequency.

With the above information, one can gain the ZPE-corrected activation energy, E_a , defined as:

$$E_a = (E_{TS} + ZPE_{TS}) - (E_{CO} + ZPE_{CO}) \quad (6)$$

where E_{TS} is the energy of the TS. Notice that the imaginary frequency of the TS is not used in the ZPE correction.

3. Results and discussion

Before tackling the adsorption of the CO molecule on the TM surfaces, one has to regard the main role-players of the adsorption process. One of these is the electronic rearrangement upon CO adsorption, summarized in the electron density donation/back-donation mechanism [38]. In this process, the CO σ -donates electron density to the TM surface, and the TM π -backdonates electron density to an antibonding orbital of the CO molecule, see Fig. 2. The electron density occupation of the CO antibonding orbital decreases its bond order, which is accompanied by a bond length elongation and a lower CO stretching vibrational frequency. Early TMs, with a high d -band centre, ϵ_d [22], are more prone to the σ -donation, and consequently, to the π -backdonation counterpart, making them better candidates for a strong CO adsorption compared to late TMs, which goes along with the calculated E_{ads} shown in Tables S4-S6 of Section S3 of the SM. Even if at this stage an E_{ads}

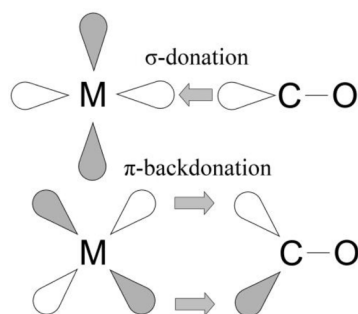


Fig. 2. Orbital scheme for the donation/back-donation mechanism of the CO interaction with a metallic M atom.

accuracy evaluation would be desirable with respect to single-crystal experimental data, the number of available reference cases is small—nine cases in the CE39 database [39]—, gained at a coverage of $\frac{1}{4}$ ML, and most of them on late *fcc* TM (111) surfaces. Neglecting lateral interaction effects, the present results yield a mean absolute error on E_{ads} of only 0.19 eV, within the standard DFT accuracy of *ca.* 0.20 eV, but such an accuracy assessment might not be representative enough, and should be taken with a grain of salt.

Focusing back on the present results analysis, the strong adsorption and electron density donation/backdonation mechanism on early TMs is directly related to the coordination number of the CO molecule on the surface, as seen in the preferred sites, listed in Tables S4-S6 of Section S3 of the SM. Those TMs with a stronger interaction tend to have a more significant number of surface TM atoms participating in the molecular coordination. Still, the σ -donation, done through the CO C atom, plus the O electron density, featuring more coulombic/steric repulsion than the C one, leads to CO molecule not being perfectly planar, see Fig. 3, but with a minor tilt, in between 53° and 72° with respect to the TM surface plane, see Tables S7-S9 of Section S4 from SM.

The enhanced molecule coordination on early TMs surfaces may lead to situations where CO molecule interacts both with surface and first subsurface layer atoms, leading to minima not originally conceived. Aside from the previous, some surfaces show certain degrees of relaxation to better accommodate the CO molecule, which may lead to significant changes, *e.g.* the relaxation in *bcc* (001) surfaces presents interlayer displacements up to 0.34 Å, and, in some cases, the TM surface may suffer of reconstructions as seen, *e.g.*, in the *hcp* ($11\bar{2}0$) surfaces from Groups III (Sc, Y) and IV (Ti, Zr, Hf) TMs. In the latest, the initial zig-zag atomic lines on the surface reconstruct to get closer to the CO molecule forming a four-atom square with the CO molecule on its centre, see Fig. 4. Such four-atom islands can be critical in the surface chemical activity, as seen in previous studies on supported TM catalysts [12,40,41]. Note that upon CO molecule removal, the four-atom islands disappear, as the surface relaxes back to its minimum.

Late TMs are very distinct from early ones due to their *d*-band being mostly or entirely full. With low *d*-band centres, ϵ_d , the electron density donation/back-donation would decrease their stability, leading to weak interactions with CO, and the corresponding attenuated coordination

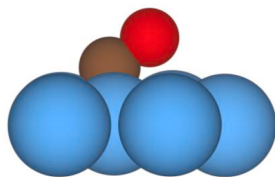


Fig. 3. Side view of CO adsorbed parallel to the Cr (011) surface, displaying the molecular tilting with respect to the metal surface plane. C and O atoms are shown as brown and red spheres, respectively, while the rest of the colour-coding is as on Fig. 1.

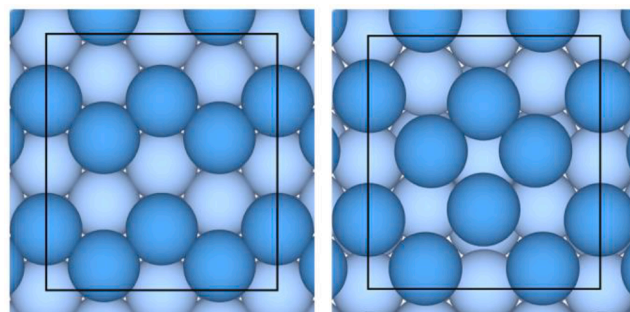


Fig. 4. Top views of an *hcp* ($11\bar{2}0$) surface before (left) and after CO adsorption induced reconstruction. CO molecule is removed for clarity. Colour code as in Fig. 1.

results in a more prone perpendicular adsorption through the C atom. Actually, for Group XII TMs (Zn, Cd), with a full *d*-band, the CO adsorption is rather weak, categorized as physisorption, see Tables S4-S6 of Section S3 from SM.

The two bonding mechanisms types are reflected in the aforementioned CO bond length, $d(\text{CO})$, elongation, and the CO stretching vibrational frequency, ν , see Tables S7-S9 of Section S4 from SM. As can be seen in Fig. 5, the $d(\text{CO})$ increases when the CO E_{ads} gets stronger, *i.e.* more negative. Notice that the overall linear regression is not perfect, but rather good, with a regression coefficient, *R*, of 0.850. When decomposing the data set according to the *bcc*, *fcc*, or *hcp* crystallographic structures, the correlation slightly increases for *hcp* and *bcc*, with *R* values of 0.854 and 0.865, but not so much for *fcc*, with *R* of 0.711. Actually, visually—one can see how the *fcc* late TMs do not show large $d(\text{CO})$ bond elongations from the initial CO molecule in vacuum value of 1.13 Å, and so does happen with late TMs with *hcp* crystallographic structure. Indeed, two sets of data could be linearly correlated depending on whether CO is perpendicular or planar, showing two clearly different trends. This picture is explained as well having a $d(\text{CO})$ linear regression with *R* = 0.765 for parallel cases, showing a more elongated bond than perpendicular cases, with an *R* of 0.719, see Fig. 5.

A similar situation is revealed on the CO stretching vibrational frequency reduction, see Fig. 6. Generally, ν decreases as the E_{ads} decreases, from an initial value of 2131 cm^{-1} for CO in vacuum. Linear trends are found accounting for all values with an *R* of 0.855, but when decomposing by crystallographic structures, only *bcc* and *hcp* retain high *R* values of 0.816 and 0.870, while *fcc* cases have an *R* of 0.552. As before,

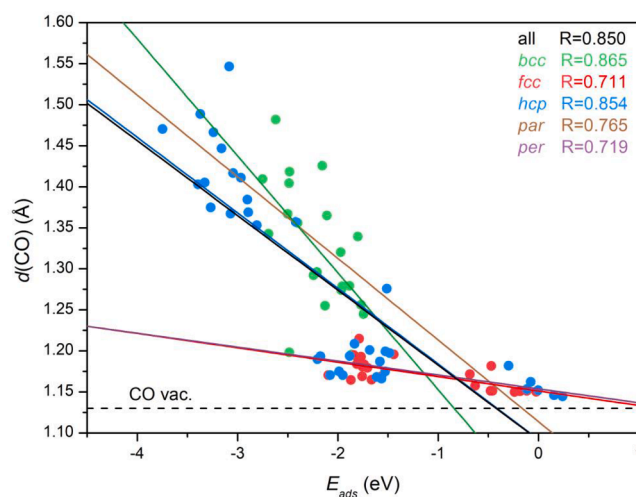


Fig. 5. Linear evolution of $d(\text{CO})$ as a function of CO E_{ads} , with all points, depending on *fcc*, *hcp*, or *bcc* crystallographic structures, of distinguishing perpendicular (*per*) and parallel (*par*) adsorptions.

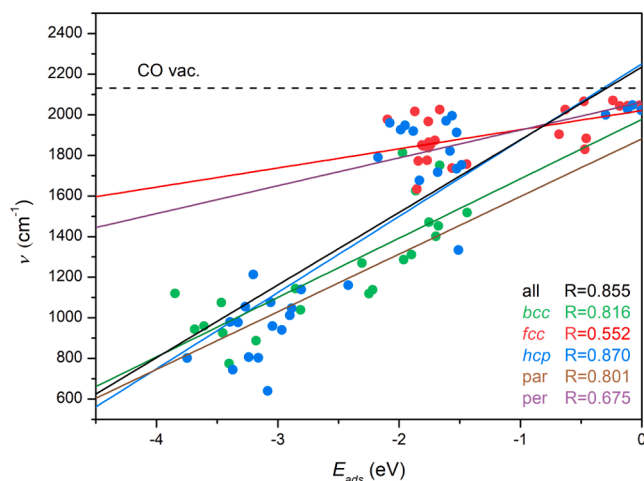


Fig. 6. Linear evolution of ν as a function of CO E_{ads} , with all points, depending on *fcc*, *hcp*, or *bcc* crystallographic structures, of distinguishing perpendicular (*per*) and parallel (*par*) adsorptions.

the two trends are clearly distinguishable depending on whether CO is perpendicular or parallel to the surface. With an R of 0.765, the parallel adsorption mode decreases the CO stretching vibrational frequency in a much more accentuated way than the perpendicular mode does, with an R of 0.719, reinforcing the idea that the bonding mechanism and bonding structure play a major role than the crystallographic phase itself.

The orientation of the adsorbed CO molecule affects not only the stretching ν value but also its simulated IR intensity, which is directly proportional to the molecular dipole moment change perpendicular to the surface associated to the vibrational motion, known as surface dipole selection rule. This makes IR-visible perpendicular motions—or with a perpendicular component—while parallel cases get their dipole moment cancelled by a mirror counterdipole generated on the underlying TM surface electronic density. This is exemplified in Fig. 7 for late, middle, and early TM surfaces with decreasing perpendicularity of the adsorbed CO molecule. The simulated IR can be found in Fig. S4 of Section S5 of the SM.

The presence of adsorbed CO still will depend on the working conditions of temperature, T , and p_{CO} . Such are accounted in the thermodynamic phase diagrams, exemplified as well in Fig. 8 for an early (Sc), middle (Fe), and late (Cu) TM, while similar behaviours can be found on

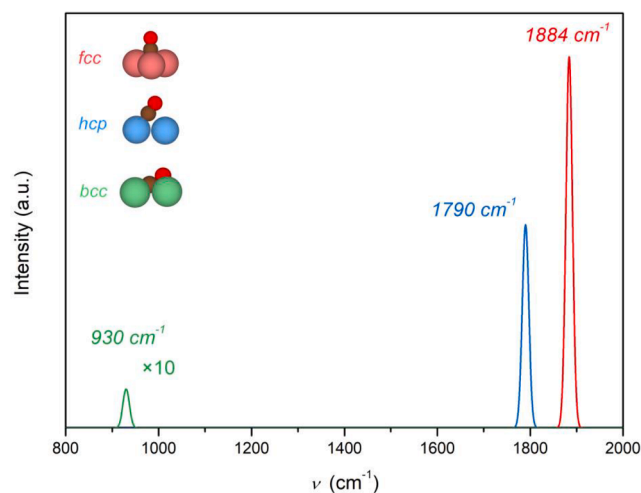


Fig. 7. Simulated IR spectra of CO adsorbed on *fcc* Au (001) surface (red), *hcp* Re (10 $\bar{1}$ 0) surface (blue), and *bcc* V (001) surface (green).

the rest of simulated thermodynamic surface phase diagrams found in Fig. S5 of Section S6 of the SM. In Fig. 8 one observes that, in general terms, for a given TM, there is a difference of CO affinity for the different explored surfaces, but that the largest effect is found when going along the d series, revealing how thermodynamic phase diagrams reduce the adsorbing regions when going for TMs with more d electrons, up to cases, like in Cu, where surfaces can reach a CO-free at high temperatures even when having a standard p_{CO} of 1 bar.

However, the above discussed trends with respect the E_{ads} are of properties of the adsorbed system. With the aim of unfolding the main descriptors involved in the interaction, this is, physicochemical properties of the pristine TM surfaces capable of predicting an adsorbate feature, an exploratory search including the d -band centre, ϵ_d , the width-corrected d -band centres, maximum Hillbert peaks of the density of states, surface energies, and workfunctions was carried out, all calculated using the same computational setup as the one here used [22,29]. Their evaluation revealed that the d -band centre [42] was the most suited choice, with an R of 0.908, see Fig. 9 and Figures S6-S9 of Section S7 of the SM.

Fig. 9 shows the linear evolution of E_{ads} as a function of ϵ_d , revealing that such a descriptor works rather well for close-packed crystallographic structures, this is, *fcc* and *hcp*, with R values of 0.916 and 0.952, respectively. However, the adequacy is lower for *bcc* TMs, with an R of 0.663. Clearly, crystal packing is a factor, but also the stacking, since the trends captured for *fcc* and *hcp* are different. The worse performance on *bcc* can be attributed to DFT lower accuracy on describing virtual orbitals or bands, whose weight is more important on early TMs ϵ_d estimates, exactly where *bcc* TMs are placed.

The adsorptive landscape for isolated C atoms was explored in earlier works using the very same TM surface models and computational setup, with the caveat that were carried out neglecting long-range interactions [43]. Thus, the most stable configurations were taken from literature and recalculated at PBE-D3 level, alongside the here calculated O adatom situations, see Tables S2-S4 of Section S2 of the SM. Such minima were used to systematically investigate the C+O coadsorptions, where sites can be found in Figures S10-S12 and values in Tables S7-S9 of Section S8 of the SM.

The C+O co-adsorption implied, in some cases, the adsorbate displacement respect the most favorable adsorption site, reducing the overall coordination number of the C+O adduct, or, in other words, diminishing the number of participating metal atoms. This is the case of C+O co-adsorption on Ir (011), see Fig. 10. The most stable position for both the C and O atom is interacting with two TM atoms in B_5 positions when they are adsorbed separately. However, the C+O coadsorption displaces the O to a Top position interacting with only one TM atom, see Fig. 10. Despite the previous, there are general similarities between the C+O co-adsorption and C and O adsorptions in terms of bonding strength and structural parameters. For instance, interaction strength for the three cases—C, O, and C+O—shows a decay of the adsorption strength along the d series. The same *hcp* (11 $\bar{2}$ 0) surface reconstruction as highlighted above is observed for Group III and IV TMs as shown in Fig. 4, only that in the C+O the C atom is located at the formed square. As found for C and O adatoms [43], and shown for CO adsorbate, the ϵ_d descriptor is the most suited as well for the C+O coadsorption, as seen in Fig. 11, where the similarity is evident, again best performing for *fcc* and *hcp* TM surfaces, with R values of 0.912 and 0.929, respectively, but with less accuracy for *bcc* TM surfaces, with an R of 0.758.

The CO dissociation leads to C+O and the feasibility of the process is determined by their difference in energy, ΔE , listed in Tables S13-S15 of Section 9 of the SM. A close inspection reveals that the CO dissociation on early TMs is exothermic, and that the exothermicity decreases when going along the d series. As above commented, early TM surfaces have the strongest donation/back-donation, substantially weakening the C—O bond, and are also eager to adsorb C and O adatom moieties upon. Altogether, both factors make the CO dissociation highly exothermic.

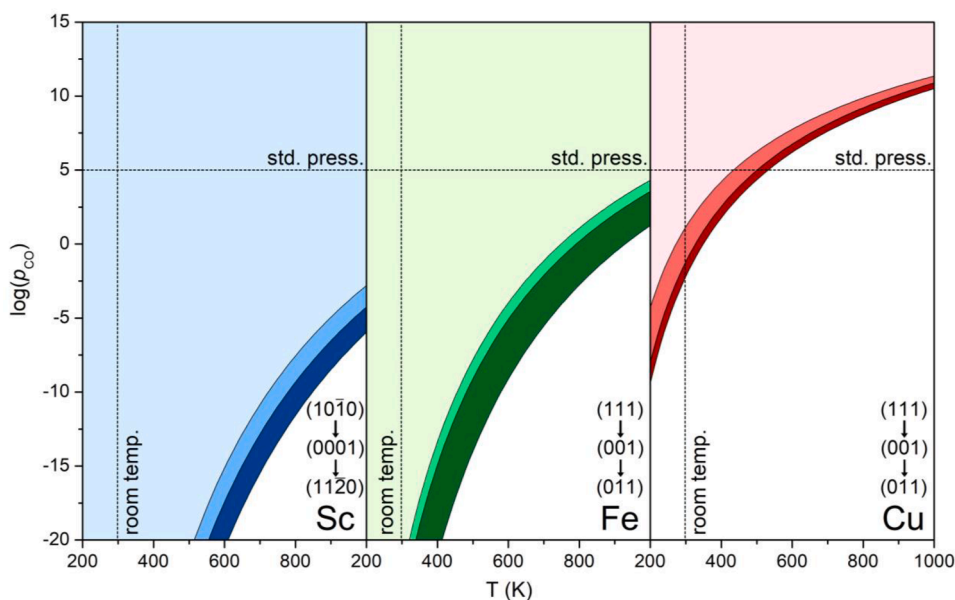


Fig. 8. Thermodynamic phase diagram for the adsorption of CO on the three explored TM surfaces of Sc (left, blue), Fe (middle, green), and Cu (right, red).

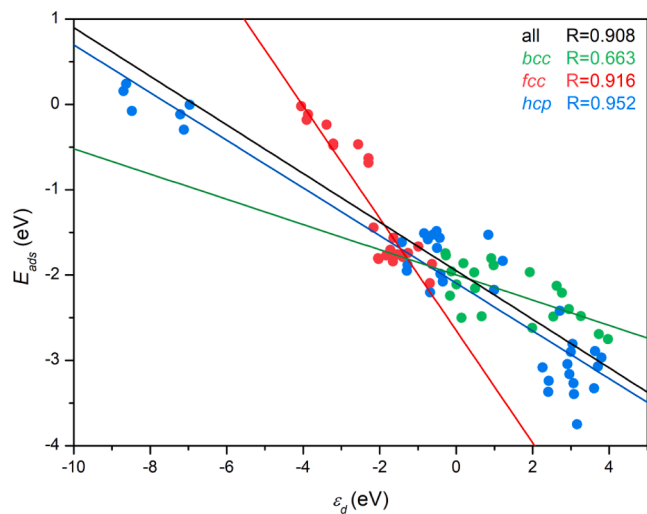


Fig. 9. Linear evolutions of CO E_{ads} vs ϵ_d descriptor, including all points, or discretizing by *fcc*, *bcc*, and *hcp* crystallographic structures.

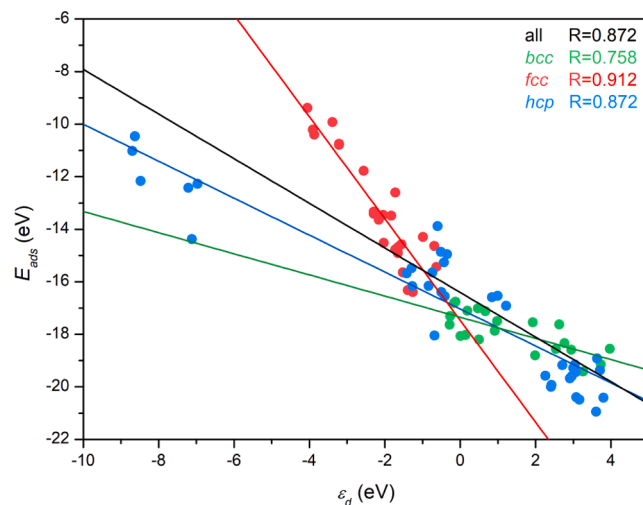


Fig. 11. Linear evolutions of C+O E_{ads} vs ϵ_d descriptor, including all points, or discretizing by *fcc*, *bcc*, and *hcp* crystallographic structures.

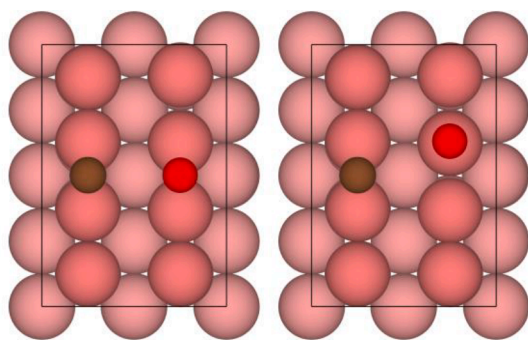


Fig. 10. Representation of the most stable position for the individual C and O atoms on Ir (011) (left) and most stable position for coadsorption (right). Colour code as in Figs. 1 and 3.

Conversely, late TM surfaces are not so active, neither to adsorb CO nor C or O adatoms, and therefore, the CO dissociation is less likely. Middle TMs from Groups VII (Tc, Re) and VIII (Fe, Ru, Os) are fringe limits for the exothermic CO dissociation, where the stability of both the reactant and the co-adsorbed C+O products is similar. In such cases, subtleties such as the TM surface ending may turn the exothermicity balance one or the other way.

Since ΔE is the difference in energy between the CO adsorbed and the C+O dissociated states, and these energies are biased by the ϵ_d descriptor, one may wonder how well the *d*-band centre describes the reaction exothermicity. Fig. 12 shows fair trends for *fcc* and *hcp* TMs, with *R* values of 0.835 and 0.868, respectively, but with a poor correlation for *bcc*, with an *R* of 0.476. Still, the representation in Fig. 12 defines different regions of thermodynamic preference towards molecular or dissociated CO on the different TM crystallographic phases. For instance, *fcc* TMs are discouraged for CO dissociation, since regularly show positive ΔE values, an only a couple of cases, Ni (001) and (011) surfaces, have ΔE values close to zero, which could be suitable for CO dissociation. Nonetheless, the CO molecule is used as a probe molecule

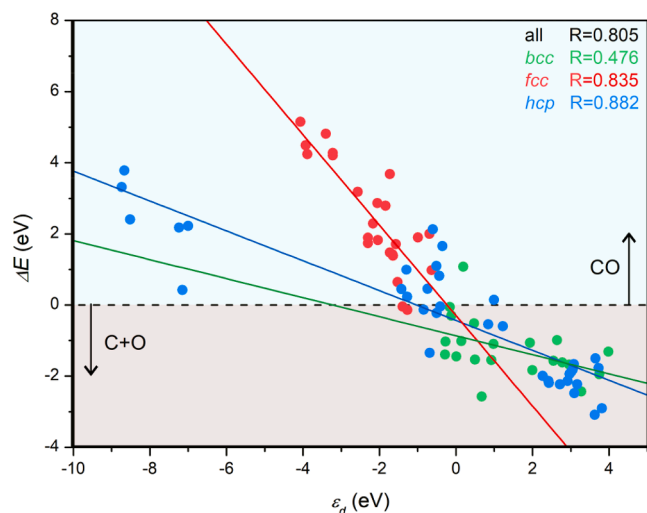


Fig. 12. Linear evolutions of CO dissociation energy change, ΔE , vs ε_d descriptor, including all points, or discretizing by *fcc*, *bcc*, and *hcp* crystallographic structures. Light green and brown denote regions of thermodynamic preference towards having adsorbed or dissociated CO.

for such late TMs [7–9], often used in catalysis, thanks to the point that the CO molecule is moderately adsorbed, but maintains its integrity, plus features normally an upright adsorption easily detectable by IR means, see Fig. 7. This would be unthinkable for *bcc* TMs, otherwise, since they normally feature negative ΔE values, except for Fe (111) surface, implying that the adsorbed CO molecule would be energetically driven to dissociate, jeopardizing the possibility of using such as a probe molecule in such metals. Finally, the *hcp* TMs display many cases distinguishable as early TMs, with $\Delta E < 0$ eV, middle TMs, with $\Delta E \sim 0$ eV, and late TMs, with $\Delta E > 0$ eV. Still, for late TMs, there are few cases with $\Delta E < 0$ eV, like Os (11 $\bar{2}$ 0) surface. Previous experimental studies [44] have shown similar qualitative trends when comparing the activity of some TM surfaces, in the sense that late TMs do not show a breakage of the CO molecule while early TMs do, and middle TMs can feature different activities on different surfaces.

Having characterized the adsorbed CO and the C+O states, the TSs for the CO dissociation process have been gained and characterized on the 81 TMs, with E_a values encompassed in Tables S13–S15 of Section S9 of the SM, and TS types listed as well, and viewed on Figures S13–S15 of Section S8 of the SM. Overall, a great diversity of E_a values have been acquired, from the very small value of 0.17 eV of *hcp* Sc (10 $\bar{1}$ 0) surface, to the very large value of 5.34 eV of *fcc* Au (111) surface. In general terms, the E_a values follow the degree of exothermicity observed in Fig. 12, i.e., the more exothermic the ΔE , the smaller the E_a . Fig. 13 shows the reaction energy profiles for three exemplary cases: The quite endothermic CO dissociation on *fcc* Au (001) surface, with an E_a of 4.95 eV, the essentially isoenergetic case of *hcp* Ru (11 $\bar{2}$ 0) surface, with an E_a of 1.38 eV, and the quite exothermic case of *bcc* V (001) surface, with a small E_a value of solely 0.45 eV. Clearly, the more exothermic the ΔE , the smaller the E_a .

Another way of analyzing the TM surface preferences towards CO dissociation is a parity plot of the energy barrier, E_a , against the CO desorption energy, seized here as minus the E_{ads} . The question mark here would be whether it would be easier for an adsorbed CO molecule to desorb or dissociate into C + O. This competitive process is represented in Fig. 14 and reveals that, on most *fcc* TM surfaces, CO would preferentially desorb, except for the Ni (001) surface. On the other hand, on most *bcc* surfaces, CO would be prompted to dissociate, except for Fe (011) and (111) surfaces. Some *bcc* TM surfaces, such as Nb and Mo (111), are in the equilibrium line where dissociation and desorption compete. Finally, as found in previous analyses, *hcp* TMs show scattered

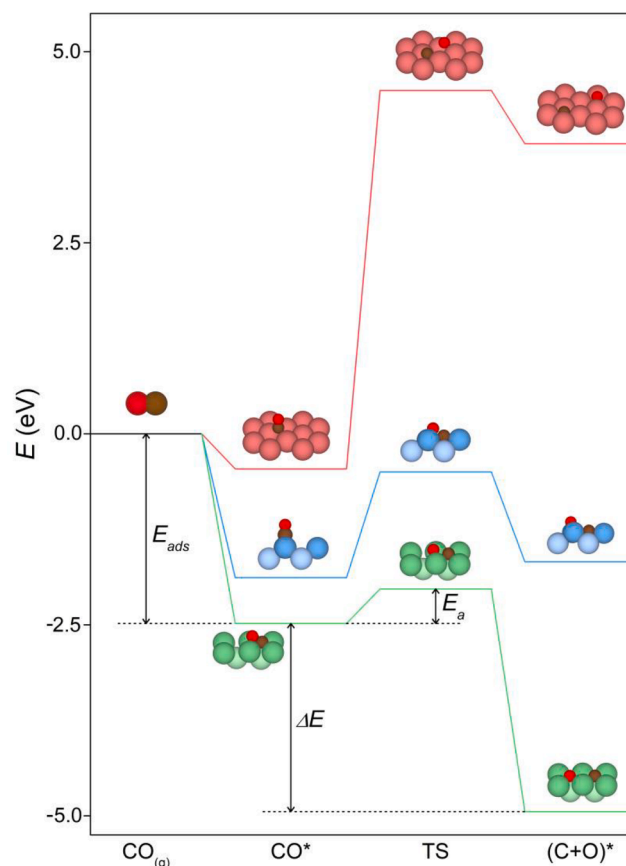


Fig. 13. Total energy reaction energy profiles for *fcc* Au (001) surface (red), *hcp* Ru (11 $\bar{2}$ 0) surface (blue), and *bcc* V (001) surface (green). Inset images denote the different stages of the reaction, going from gas phase CO, $\text{CO}^{(g)}$, to adsorbed CO, CO^* , the CO dissociation TS, and the coadsorbed C+O, $(\text{C}+\text{O})^*$. Colour coding as in Figs. 1 and 3.

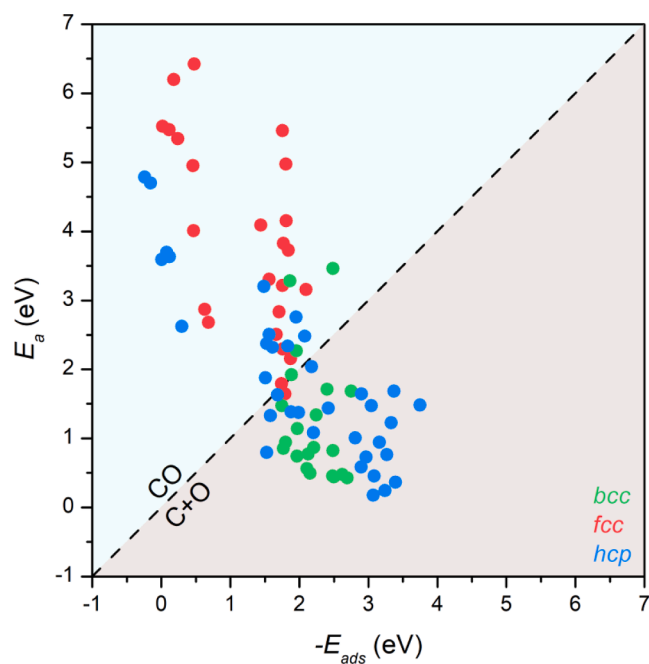


Fig. 14. Activation energy, E_a , for the CO dissociation vs the desorption energy, $-E_{ads}$. The dashed line are situations where $E_a = -E_{ads}$. Colour coding as in Fig. 11.

trends depending on whether it is an early, middle, or late TM. It is worth mentioning that Tc (11 $\bar{2}$ 0) and Re (0001) surfaces, which would walk the parity line, where both CO desorption and dissociation are kinetically equally likely.

Fig. 15 qualitatively assess whether the reaction energy barrier, E_a , is also defined by ε_d , like the molecular and atomic E_{ads} as found above. The plot shows how *fcc* has a different behaviour when compared to *hcp* and *bcc*, and the better linearity for close-packed crystallographic phases than for *bcc* TMs. Figs. 9, 11, and 12 illustrate that, in general, ε_d defines the reactants and products adsorption energies, and these, in turn, define the reaction energy difference, ΔE . The reaction energy also conditions the extent of the reaction energy barrier, E_a , aligned with the Brønsted-Evans-Polanyi (BEP) relationships [45,46].

The BEP is indeed evaluated in Fig. 16. Notice that two limits define a $E_a/\Delta E$ region where a BEP is possible. One is a limit case for earliest TSS—located very close to the reactants energy level—where there is essentially no energy barrier, regardless the value ΔE has, i.e. $E_a = 0$ eV, and so, basically the linear equation of $E_a = a \cdot \Delta E + b$ has a slope a of zero, and a b intercept of 0. On the other hand, latest TSS—located very close to the products energy level—are significant for endothermic situations, where the energy barrier is basically the difference in energy between reactants and products, i.e. $E_a = \Delta E$, and so, basically, the linear equation of $E_a = a \cdot \Delta E + b$ has a slope a of one, and a b intercept of 0.

Within these limits, one may plot the obtained pairs of E_a and ΔE , as shown in Fig. 16. Notice how the gained BEP relation is good with a regression coefficient R of 0.899, even if mixing different surface terminations crystallographic structures, and reaction mechanisms, see Fig. 13, and as good as a descriptor as the ε_d , shown in Fig. 14, underscoring that ε_d is, perchance, a suited descriptor of the TMs surfaces chemical activity, and, in an indirect way, of the chemical reactivity, as ΔE does. Aside, the BEP slope of 0.667 is in between the limits of 0 and 1, implying that is not simply defined by ΔE , but also other TM surface factors play a role in the TS definition and the estimate of the E_a .

Reached this point, and considering all the above data, one may wonder which TM surface would be best for the CO dissociation. To this end, one has to keep in mind that optimal E_a and ΔE values for this step would be essentially zero for both, implying that such a reaction step would not be a reaction-determining step at any working conditions, and more regarded as a free step, where no energetic toll has to be paid. Large E_a values, even when having quite exothermic ΔE values, would be thermodynamically driven steps, that would be kinetically hindered. On the other hand, low E_a values with quite exothermic ΔE s would be

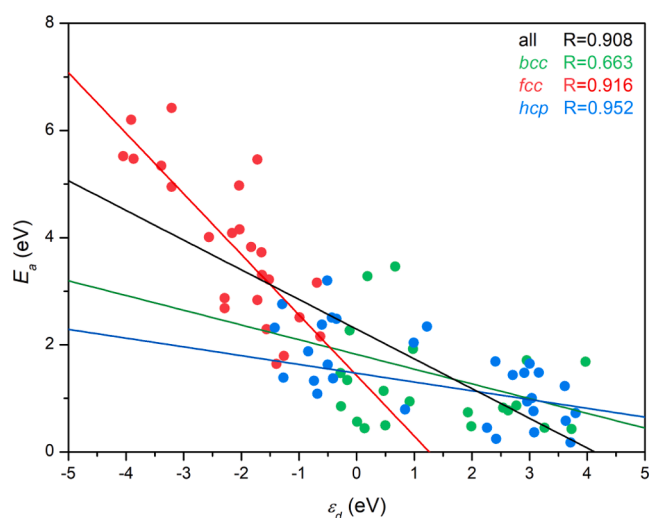


Fig. 15. Linear evolutions of CO activation energy change, E_a , vs ε_d descriptor, including all points, or distinguishing by *fcc*, *bcc*, and *hcp* crystallographic structures.

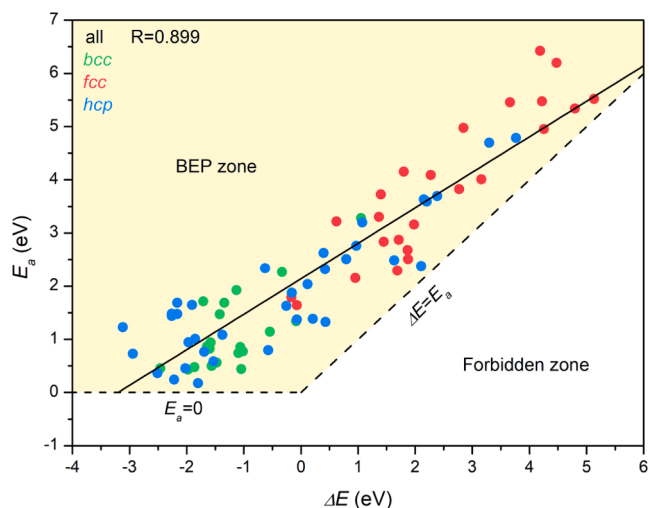


Fig. 16. BEP relationship for CO dissociation on TMs, showing the crystallographic distribution, and the BEP space. Dashed lines illustrates the BEP limits for $E_a = 0$ eV, and $E_a = \Delta E$, highlighted in yellow. The forbidden zone notes the region where there is either $E_a < 0$ eV or $E_a < \Delta E$, which are impossible situations where no data should be observed.

suitable steps, but with the concomitant danger of falling into a reaction energy pit, where it would be difficult to make react or remove the C and O adatoms products.

As stated by the *Le Sabatier* principle, a good catalyst material attaches moieties upon neither too weakly nor too strongly. Thus, in practice, low E_a with slightly exothermic ΔE s are best compromises, and, actually, research endeavours are being carried out at systems breaking such linear behaviour relations, e.g. using single-atom alloys in TMs [47]. This restricts the search for ΔE s < 0 eV, and in the low part of the BEP. With this guideline in mind, one TM surface outstands; the *hcp* Re (11 $\bar{2}$ 0) surface, with an E_a of 0.79 eV and a ΔE of -0.57 eV. Actually, Re has been regarded as a suited additive to Co to improve the FT performance, where CO dissociation is regarded as a possible rate-limiting step [48]. Other TMs could be used for breaking the CO in a suited fashion, e.g. the *bcc* Fe (001) surface, with an E_a of 1.14 eV and a ΔE of -0.54 eV, the *hcp* Os (11 $\bar{2}$ 0) surface, with an E_a of 1.37 eV and a ΔE of -0.07 eV, the *hcp* Co (11 $\bar{2}$ 0) surface, with an E_a of 1.32 eV and a ΔE of 0.42 eV, and the *hcp* Ru (11 $\bar{2}$ 0) surface, with an E_a of 1.38 eV and a ΔE of 0.20 eV, and such TMs coincide with the FT commercial catalysts, formed by TM of groups VII (Re), VIII (Fe, Ru, Os), and IX (Co) [49–51].

Notice that in the above highlighted cases, except for Fe (001) surface, all are *hcp* (11 $\bar{2}$ 0) surfaces. This underscores how the surface geometry seems to be crucial to promote the CO dissociation. The (11 $\bar{2}$ 0) surfaces, compared to the (0001) and (10 $\bar{1}$ 0) ones, have an atomic layout that permits a higher coordination towards the CO adsorbate, effectively fostering the interaction, thus, weakening the CO bond and allowing for a better dissociation. However, the *hcp* (11 $\bar{2}$ 0) surfaces are the least stable ones according to their surface energies, which in turn explains in part their enhanced chemical activity [29]. This surface has to be engineered in any Re, Os, Co, or Ru catalyst that such surface sites have to be engineered, e.g. through nanostructuring, or using capping agents during the TM catalyst formation.

4. Conclusions

The adsorption of CO and coadsorption of C and O adatoms on 81 TM surfaces have been studied by DFT means in order to elucidate main trends governing the CO surface stability and TM surface dissociation reactivity along series, groups, surface terminations, and crystallographic phases. The CO adsorption has shown clear trends relating its

strength with the TMs conforming the surface. Early TMs, such as *bcc* TMs, with emptier *d*-bands, tend to feature a strong interaction in less restricted conditions involving more surface metal atoms and having the CO adsorbed in a more planar way, increasing the CO bond length, *d* (CO), and significantly reducing CO stretching frequency, ν , which, nevertheless, is quite invisible under IR spectroscopy.

On the other extreme, late TMs, such as *fcc* TMs, involve fewer surface metal atoms coordinating the CO molecule, which adsorbs perpendicularly with a moderate strength and more restricted conditions. The *d*(CO) and ν are slightly increased and decreased, respectively, but the stretching frequency ν would be visible under IR radiation spectroscopy. Finally, *hcp* TMs, having early, middle, and late cases, show the two just explained behaviours, plus cases laying in between. Both *d*(CO) and ν features reveal clear distinct trends with respect the CO adsorption energy according to whether it is adsorbed perpendicular or parallel to the TM surface.

The CO adsorption and C+O coadsorption energies show similar trends best described though through the *d*-band centre, almost quantitatively for *hcp* and *fcc* TMs, but with ϵ_d descriptor poorly describing *bcc* TMs. Such trends are also observed on CO dissociation ΔE vs ϵ_d , revealing that such a reaction is highly endothermic for a series of TMs, mostly *fcc* late TMs, excessively exothermic for another series of TMs, mostly *bcc* TMs, while *hcp* values are spread; only those TMs of Groups VII, VIII, and IX feature moderate ΔE values adequate for the catalysis involving the CO dissociation, while late TMs are thus more suited when involving a catalysis where the CO integrity needs to be maintained, e.g. in the course of CO₂ hydrogenation towards methanol, carried out in Groups IX (Rh, Ir), X (Ni, Pd, Pt), and XI (Cu, Ag, Au) [51–57].

The dissociation energy barriers follow a BEP relation with respect ΔE , and are also defined by ϵ_d descriptor. The competition of CO desorption vs the CO dissociation also yields the same conclusions as the ΔE and BEP analyses. Group VII (Re), VIII (Fe, Ru, Os), and IX (Co) TMs are the most suited to catalyse the CO dissociation, in line with the FT performance. However, while in the case of Fe could be a regular (001) surface, on Re, Ru, Os, and Co the best performance would be, *a priori*, on (11 $\bar{2}$ 0) surface, which is the least stable one. Thus, the study concludes that such TM systems displaying (11 $\bar{2}$ 0) facets could have a better CO dissociation catalytic activity, useful, e.g. for FT, better than other more stable surfaces. On the other hand, late *fcc* TM surfaces are more adequate for keeping the CO integrity and are better suited for other types or reactions, such as the methanol synthesis. These obtained trends may aid future studies in order to understand the behaviour of other high Miller indices surfaces or vicinal surfaces, or more complex systems such as bimetallic surfaces or single TM atom catalysts.

CRediT authorship contribution statement

David Vázquez-Parga: Visualization, Validation, Investigation, Software, Data curation, Formal analysis, Writing – original draft. **Anabel Jurado:** Visualization, Validation, Investigation, Software, Data curation, Formal analysis, Writing – review & editing. **Alberto Roldan:** Conceptualization, Supervision, Formal analysis, Writing – review & editing, Resources, Funding acquisition, Project administration. **Francisco Viñes:** Conceptualization, Supervision, Formal analysis, Writing – review & editing, Resources, Funding acquisition, Project administration.

Declaration of Competing Interest

The authors declare that they have no known competing financial interests or personal relationships that could have appeared to influence the work reported in this paper.

Data availability

Data will be made available on request.

Acknowledgements

This research stay was carried out financed through and thanks the HPC-Europa3 programme, with project ID INFRAIA-2016-1-730897, and also with the support of the EC Research Innovation Action under the H2020 Programme of the European Union (EU). We also acknowledge Supercomputing Wales for access to the Hawk HPC facility, part-funded by the European Regional Development Fund via the Welsh Government, and the computer resources and technical support provided by the supercomputer ARCHER2. The research carried out at the *Universitat de Barcelona* has been supported by the Spanish MCIN/AEI/10.13039/501100011033 funded RTI2018-095460-B-I00, PID2021-126076NB-I00, and *María de Maeztu* MDM-2017-0767 grants. Supercomputing time is acknowledged to the *Red Española de Supercomputación* (RES) through granted projects QHS-2022-1-0010 and QHS-2022-2-0014.

Appendix A. Supplementary material

Supplementary data to this article can be found online at <https://doi.org/10.1016/j.apsusc.2023.156581>.

References

- [1] E. Pomerantseva, F. Bonaccorso, X. Feng, Y. Cui, Y. Gogotsi, Energy storage: The future enabled by nanomaterials, *Science* 336 (2019) eaan8285.
- [2] M. Kumar, K. Raza, C₆₀-fullerenes as drug delivery carriers for anticancer agents: Promises and hurdles, *Pharm. Nanotechnol.* 5 (2017) 169–179.
- [3] F. Viñes, J.R.B. Gomes, F. Illas, Understanding the reactivity of metallic nanoparticles: beyond the extended surface model for catalysis, *Chem. Soc. Rev.* 43 (2014) 4922–4939.
- [4] M.A. Babaeva, D.S. Bystrov, A.Y. Kovalgin, A.A. Tsyganenko, CO interaction with the surface of thermally activated CaO and MgO, *J. Catal.* 123 (1990) 396–416.
- [5] E. Jerero, V. Labarbier, A. Datye, Y. Wang, J.M. Vohs, Interaction of CO with surface PdZn Alloys, *Surf. Sci.* 601 (2007) 5546–5554.
- [6] K. Bleakley, P.A. Hu, Density Functional Theory Study of the Interaction between CO and O on a Pt Surface: CO/Pt(111), O/Pt(111), and CO/O/Pt(111), *J. Am. Chem. Soc.* 121 (1999) 7644–7652.
- [7] C.J. Weststrate, E. Lundgren, J.N. Andersen, E.D.L. Rienks, A.C. Gluhoi, J. W. Bakker, I.M.N. Groot, B.E. Nieuwenhuys, CO adsorption on Au(310) and Au(321): 6-Fold coordinated gold atoms, *Surf. Sci.* 603 (2009) 2152–2157.
- [8] J. Pischel, A. Pucci, Low-temperature adsorption of carbon monoxide on gold surfaces: IR spectroscopy uncovers different adsorption states on pristine and rough (111), *J. Phys. Chem. C* 119 (2015) 18340–18351.
- [9] H.J. Yang, T. Minato, M. Kawai, Y. Kim, STM Investigation of CO Ordering on Pt(111): from an isolated molecule to high-coverage superstructures, *J. Phys. Chem. C* 117 (2013) 16429–16437.
- [10] L. Fajín, M.N. Cordeiro, J.R.B. Gomes, Fischer-tropsch synthesis on multicomponent catalysts: what can we learn from computer simulations? *Catalysts* 5 (2015) 3–17.
- [11] NIST Computational Chemistry Comparison and Benchmark Database. NIST Standard Reference Database Number 101. <http://cccbdb.nist.gov>.
- [12] S. Posada-Pérez, P.J. Ramírez, R.A. Gutiérrez, D.J. Stacchiola, F. Viñes, P. Liu, F. Illas, J.A. Rodríguez, The conversion of CO₂ to methanol on orthorhombic β -Mo₂C and Cu/ β -Mo₂C catalysts: mechanism for admetal induced change in the selectivity and activity, *Catal. Sci. Technol.* 6 (2016) 6766–6777.
- [13] G. Mpourmpakis, A.N. Andriotis, D.G. Vlachos, Identification of Descriptors for the CO Interaction with Metal Nanoparticles, *Nano Lett.* 10 (2010) 1041–1045.
- [14] L. Vega, J. Garcia-Cardona, F. Viñes, P.L. Cabot, K.M. Neyman, Nanostructuring determines poisoning: tailoring CO adsorption on PtCu bimetallic nanoparticles, *Mater. Adv.* 3 (2022) 4159–4169.
- [15] D.R. Pye, N.P. Mankad, Bimetallic catalysis for C-C and C-X coupling reactions, *Chem. Sci.* 8 (2017) 1705–1718.
- [16] R.T. Hannagan, G. Giannakakis, M. Flytzani-Stephanopoulos, E.C.H. Sykes, Single-Atom Alloy Catalysis, *Chem. Rev.* 120 (2020) 12044–12088.
- [17] A.A. Peterson, L.C. Grabow, T.P. Brennan, B. Shong, C. Ooi, D.M. Wu, C.W. Li, A. Kushwaha, A.J. Medford, F. Mbuga, L. Li, J. Nørskov, Finite-Size Effects in O and CO Adsorption for the Late Transition Metals, *Top. Catal.* 55 (2012) 1276–1282.
- [18] J. Ruvireta, L. Vega, F. Viñes, Cohesion and coordination effects on transition metal surface energies, *Surf. Sci.* 664 (2017) 45–49.
- [19] G. Kresse, J. Furthmüller, Efficiency of ab-initio total energy calculations for metals and semiconductors using a plane-wave basis set, *Comput. Mat. Sci.* 6 (1996) 15–50.

- [20] G. Kresse, D. Joubert, From ultrasoft pseudopotentials to the projector augmented-wave method, *Phys. Rev. B* 59 (1999) 1758–1775.
- [21] J.P. Perdew, K. Bruke, M. Ernzerhof, Generalized Gradient Approximation Made Simple, *Phys. Rev. Lett.* 77 (1996) 3865.
- [22] L. Vega, B. Martínez, F. Viñes, F. Illas, Robustness of surface activity electronic structure-based descriptors of transition metals, *Phys. Chem. Chem. Phys.* 20 (2018) 20548–20554.
- [23] S. Grimme, J. Anthony, S. Ehrlich, H. Krieg, A consistent and accurate ab initio parametrization of density functional dispersion correction (DFT-D) for the 94 elements H-Pu, *J. Chem. Phys.* 132 (2010), 154104.
- [24] A. Tkatchenko, A.R. DiStasio, R. Jr, M.S. Car, Accurate and efficient method for many-body van der waals interactions, *Phys. Rev. Lett.* 108 (2012), 236402.
- [25] R.B. Araujo, G.L.S. Rodrigues, E.C. dos Santos, L.G.M. Pettersson, Adsorption energies on transition metal surfaces: towards an accurate and balanced description, *Nat. Commun.* 13 (2022) 6853.
- [26] P.J. Feibelman, B. Hammer, J.K. Nørskov, F. Wagner, M. Scheffler, R. Stumpf, R. Watwe, J. Dumesic, The CO/Pt(111) Puzzle, *J. Phys. Chem. B* 105 (2001) 4018–4025.
- [27] A. Gil, A. Clotet, J.M. Ricart, G. Kresse, M. García-Hernandez, N. Rösch, P. Sautet, Site Preference of CO Chemisorbed on Pt(111) from Density Functional Calculations, *Surf. Sci.* 530 (2003) 71–87.
- [28] P. Janthon, F. Viñes, J. Sirjaraense, J. Limtrakul, F. Illas, Adding Pieces to the CO/Pt(111) Puzzle: the role of dispersion, *J. Phys. Chem. C* 121 (2017) 3970–3977.
- [29] L. Vega, J. Ruviera, F. Viñes, F. Illas, Jacob's Ladder as Sketched by Escher: assessing the performance of broadly used density functionals on transition metal surface properties, *J. Chem. Theory Comput.* 14 (2018) 395–403.
- [30] B. Shan, Y. Zhao, J. Hyun, N. Kapur, J.B. Nicholas, K. Cho, Coverage-Dependent CO adsorption energy from first-principles calculations, *J. Phys. Chem. C* 113 (2009) 6608–66092.
- [31] T. Wang, X.-X. Tian, Y.-W. Li, J. Wang, M. Beller, H. Jiao, Coverage-Dependent CO adsorption and dissociation mechanisms on iron surfaces from DFT computations, *ACS Catal.* 4 (2014) 1991–2005.
- [32] M. Happel, N. Luckas, F. Viñes, M. Sobota, M. Laurin, A. Görling, J. Libuda, SO₂ Adsorption on Pt(111) and Oxygen Precovered Pt(111): a combined infrared reflection absorption spectroscopy and density functional study, *J. Phys. Chem. C* 115 (2011) 479–491.
- [33] F. Viñes, A. Iglesias-Juez, F. Illas, M. Fernández-García, Hydroxyl Identification on ZnO by infrared spectroscopies: theory and experiments, *J. Phys. Chem. C* 118 (2014) 1492–1505.
- [34] S. Campisi, C. Beevers, A. Nasrallah, C.R.A. Catlow, C.e. Chan-Thaw, M. Manzoli, N. Dimitratos, D.J. Willock, A. Roldan, A. Villa, DFT-Assisted Spectroscopic Studies on the Coordination of Small Ligands to Palladium: From Isolated Ions to Nanoparticles, *J. Phys. Chem. C* 124 (2020) 4781–4790.
- [35] O. Piqué, I.Z. Koleva, F. Viñes, H.A. Aleksandrov, G.N. Vayssilov, F. Illas, Subsurface carbon: a general feature of noble metals, *Angew. Chem. Int. Ed.* 58 (2019) 1744–1748.
- [36] G. Henkelman, H. Jónsson, A dimer method for finding saddle points on high dimensional potential surfaces using only first derivatives, *Chem. Phys.* 111 (1999) 7010.
- [37] G. Henkelman, B.P. Uberuaga, H. Jónsson, A climbing image nudged elastic band method for finding saddle points and minimum energy paths, *J. Chem. Phys.* 113 (2000) 9901.
- [38] F. Ample, D. Curulla, F. Fuster, A. Clotet, J.M. Ricart, Adsorption of CO and CN⁻ on transition metal surfaces: a comparative study of the bonding mechanism, *Surf. Sci.* 497 (2002) 139–154.
- [39] J. Wellendorf, T.L. Silbaugh, D. Garcia-Pintos, J.K. Nørskov, T. Bligaard, F. Studt, C.T. Campbell, A benchmark database for adsorption bond energies to transition metal surfaces and comparison to selected DFT functionals, *Surf. Sci.* 640 (2015) 36–44.
- [40] J.A. Rodriguez, P.J. Ramirez, G.G. Asara, F. Viñes, J. Evans, P. Liu, J.M. Ricart, F. Illas, Charge Polarization at a Au–TiC Interface and the generation of highly active and selective catalysts for the low-temperature water-gas shift reaction, *Angew. Chem. Int. Ed.* 53 (2014) 11270–11274.
- [41] H. Prats, P.A. Gutiérrez, J.J. Piñero, F. Viñes, S.T. Bromley, P.J. Ramirez, J. A. Rodriguez, F. Illas, Room temperature methane capture and activation by Ni Clusters Supported on TiC(001): effects of metal-carbide interactions on the cleavage of the C-H Bond, *J. Am. Chem. Soc.* 141 (2019) 5303–5313.
- [42] B. Hammer, J.K. Nørskov, Electronic factors determining the reactivity of the metal surfaces, *Surf. Sci.* 343 (1995) 211–220.
- [43] O. Piqué, I.Z. Koleva, A. Bruix, F. Viñes, H.A. Aleksandrov, G.N. Vayssilov, F. Illas, Charting the Atomic C Interaction with transition metal surfaces, *ACS Catal.* 12 (2022) 9256–9269.
- [44] G. Brodén, T.N. Rhodin, C. Brucker, R. Benow, Z. Hurych, Synchrotron radiation study of chemisorptive bonding of CO on transition metals – polarization effect on Ir(100), *Surf. Sci.* 59 (1976) 593–611.
- [45] J.N. Brønsted, Acid and Basic Catalysis, *Chem. Rev.* 5 (1928) 231–338.
- [46] M.G. Evans, M. Polanyi, Inertia and driving force of chemical reactions, *Trans. Faraday Soc.* 34 (1938) 11–24.
- [47] M.T. Darby, M. Stamatakis, A. Michaelides, E.C.H. Sykes, Lonely Atoms with Special Gifts: breaking linear scaling relationships in heterogeneous catalysis with single-atom alloys, *J. Phys. Chem. Lett.* 9 (2018) 5636–5646.
- [48] E.Y. Asaliev, E.V. Kul'chakovskaya, L.V. Sineva, V.Z. Mordkovich, Effect of rhenium on Fischer-Tropsch synthesis in the presence of cobalt–zeolite catalysts, *J. Pet. Chem.* 57 (2017) 251–256.
- [49] J. Cheng, P. Hu, P. Ellis, S. French, G. Kellyc, C.M. Martin, A DFT study of the chain growth probability in Fischer-Tropsch synthesis, *J. Catal.* 257 (2008) 221–228.
- [50] T. Molefe, R.P. Forbes, N.J. Coville, Osmium@hollow Carbon Spheres as Fischer-Tropsch Synthesis Catalysts, *Catal. Lett.* 151 (2021) 875–887.
- [51] S. Sugawa, K. Sayama, K. Okabe, H. Arakawa, Methanol synthesis from CO₂ and H₂ over silver catalyst, *Manag.* 36 (1995) 665–668.
- [52] L.C. Grabow, M. Mavrikakis, Mechanism of methanol synthesis on Cu through CO₂ and CO Hydrogenation, *ACS Catal.* 1 (2011) 365–384.
- [53] A.B. Vidal, L. Feria, J. Evans, Y. Takahashi, P. Liu, K. Nakamura, F. Illas, J. A. Rodriguez, CO₂ Activation and methanol synthesis on novel Au/TiC and Cu/TiC Catalysts, *J. Phys. Chem. Lett.* 3 (2012) 2275–2280.
- [54] J. Xu, X. Su, X. Liu, X. Pan, G. Pei, Y. Huang, X. Wang, T. Zhang, H. Geng, Methanol synthesis from CO₂ and H₂ over Pd/ZnO/Al₂O₃: Catalyst structure dependence of methanol selectivity, *Appl. Catal. A: Gen.* 514 (2016) 51–59.
- [55] E.S. Gutterød, A. Lazzarini, T. Fjermestad, G. Kaur, M. Manzoli, S. Bordiga, S. Svelle, K.P. Lillerud, E. Skúlason, S. Øien-Ødegaard, A. Nova, U. Olsbye, Hydrogenation of CO₂ to Methanol by Pt Nanoparticles Encapsulated in UiO-67: deciphering the role of the metal-organic framework, *J. Am. Chem. Soc.* 142 (2020) 999–1009.
- [56] G. Peng, L. Xu, V.A. Glezakou, M. Mavrikakis, Mechanism of methanol synthesis on Ni(110), *Catal. Sci. Technol.* 11 (2021) 3279–3294.
- [57] F. Geng, X. Zhan, J.C. Hicks, Promoting methanol synthesis and inhibiting CO₂ Methanation with Bimetallic In–Ru Catalysts, *ACS Sustainable Chem. Eng.* 9 (2021) 11891–11902.